Electronic Supplementary Material (ESI) for Materials Horizons.
This journal is © The Royal Society of Chemistry 2018

Experimental section

Chemicals and materials. Aniline ($C_6H_5NH_2$, JIS Special Grade), Nitric acid (HNO_3, JIS Special Grade), Hydrochloric acid (HCl, JIS Special Grade), Sulfuric acid (H_2SO_4, JIS Special Grade), Potassium hydroxide (KOH, JIS Special Grade) and Phosphomolybdic acid ($H_3PMo_{12}O_{40}$) were purchased from Wako Pure Chemical Industries, Ltd. Potassium hexacyanoferrate(III) ($K_3[Fe(CN)_6]$, JIS Special Grade) was purchased from nacalai tesque. Potassium hexacyanocobaltate(III) ($K_3[Co(CN)_6]$, >97.0%), Potassium tetracyanonickelate(II) hydrate ($K_2[Ni(CN)_4]\bullet xH_2O$, 98%), Ammonium tetrathiomolybdate ($(NH_4)_2MoS_4$, >99.9%), Potassium tetracyanoplatinate(II) ($K_2[Pt(CN)_4]$, 98.0%), and commercial Pt/C (20 wt%) was purchased from Sigma-Aldrich. Nafion solution (5 wt%) was purchased from DuPont. Carbon paper (CP) was provided by Toray (Japan).

Synthesis of catalysts. The preparation of PANI polymer with hierarchical structure was achieved *via* the electrodeposition method using a three-electrode system. Carbon paper (2.5×4 cm^2) was firstly treated at 500 ^oC in air for 1.5 h and washed with concentrated acid. The treated carbon paper was used as working electrode and counter electrode and saturated calomel electrode (SCE) was used as reference electrode. The electrolyte was prepared by dissolving 7.4 mL HNO_3 in 88 mL H_2O and then adding 4.6 mL aniline to form uniform solution after stirring for half an hour. The in situ electrochemical polymerization of PANI was carried out by galvanostatic method at a current density of 2 mA cm^{-2} for 4000 s on CP electrode. After that, PANI/CP was washed with water, followed by drying at 80 ^oC for 1 h. To investigate the anionic effect, HCl, H_2SO_4, and H_3PO_4 were also used for the synthesis of PANI at the same conditions with keeping the acid concentration of 1 M. The electrochemical redox behavior of the PANI polymer was evaluated through CV in a 0.5 M HNO_3 electrolyte by using a three-electrode system. The redox states were tailored by the potentiostatic method. The samples were treated at selected potentials for 0.5 h and then immersed in 50 mL water for 1h. Next, metal complex solution was prepared by dissolving 0.5 mmol $K_3[Co(CN)_6]$ in 80 mL H_2O and the different potentials treated PANIs were added in the solution for 1h under stirring. After a full adsorption, metal complex/PANI composites were washed three times and dried in vacuum oven 50 ^oC for 1 h. Finally, the composite precursors were carbonized at 900 ^oC in N_2 atmosphere for 3 h. The obtained samples were termed as Co@NC(x), where x was the applied potentials on PANI precursor. The mass loading of Co modified carbon is determined by the mass difference before and after the synthesis using a microbalance. In order to prove the universality of this method, Ni@NC, Fe_3O_4/Fe_3C@NC, amorphous MoC_xS_y@NC, MoC@NC, and Pt@NC hybrids were also prepared by simply replacing the $K_3[Co(CN)_6]$ with $K_2[Ni(CN)_4]\bullet xH_2O$, $K_3[Fe(CN)_6]$, $(NH_4)_2MoS_4$, $H_3PMo_{12}O_{40}$, and $K_2[Pt(CN)_4]$. The treatment conditions are a little different from Co@NC. For Ni@NC and Fe_3O_4/Fe_3C@NC, the carbonization condition was 700 ^oC in N_2 atmosphere for 2 h. For MoC_xS_y@NC, the carbonization condition was 1000 ^oC in N_2 atmosphere for 3 h. For MoC@NC, the carbonization condition was 800 ^oC in N_2 atmosphere for 6 h. For Pt@NC, the PANI deposition time was shortened to 1200s and the carbonization condition was 700 ^oC in N_2 atmosphere for 3 h.

Materials characterization. The morphology was observed with scanning electron microscopy (SEM, HITACHI S-4800) operated at 10 kV. Transmission electron microscopy (TEM), scanning transmission electron microscopy (STEM) images, energy-dispersive X-ray spectroscopy (EDXS), and elemental mapping analysis were performed using a JEM-2100F (JEOL) operated at 200 kV. The thermal properties of the precursors were assessed with a thermogravimetric analysis (6300TG/DTA, Hitachi HT-Seiko Instrument Exter) under N□$_2$ atmosphere. Powder X-ray diffraction (XRD) was performed on a Rigaku RINT 2000X-ray diffractometer with monochromated Cu Kα radiation (40 kV, 40 mA). Raman spectra were measured and collected using a 532 nm laser by a RAMAN-11 (nano photon). X-ray photoelectronic spectroscopy (XPS) spectra were carried out by using a PHI Quantera SXM (ULVAC-PHI) instrument with an Al Kα X-ray source. All the binding energies were calibrated via referencing to C 1 s binding energy (285.0 eV). Inductively coupled plasma atomic emission spectroscopy (ICP-AES) measurements were performed on HITACHI High-Technologies Corporation model SPS3520UV-DD. Nitrogen adsorption-desorption isotherms were obtained by using a Belsorp 28 apparatus (Bel Japan, Inc.) to investigate the surface area of the hybrids by Multipoint Brunauer-Emmett-Teller(BET) methods.

Electrocatalysis measurements. The electrochemical experiments for HER were carried out with a CHI 660D (ALS, Japan) at room temperature using a three-electrode configuration with as-prepared electrodes, graphite plate and saturated calomel electrode (SCE) as working electrode, counter electrode and reference electrode, respectively. The as-prepared samples were directly used as working electrodes without any treatment. The polarization curves were obtained in 1 M KOH with a scan rate of 5 mV s^{-1} at room temperature. As two examples, the HER performance of Co@NC and Pt@NC samples were systematically investigated. The mass loadings for Co@NC were around 1.7 mg cm^{-2}, respectively. The mass loadings for Pt@NC were around 0.6 mg cm^{-2}, respectively. For powder samples, the working electrode was prepared by mixing powder and nafion (9 : 1 in weight ratio) in 1 mL ethanol solvent. After sonication for 30 min, the slurry was coated onto carbon paper (1 × 0.5 cm^2, Toray, Japan), and dried at room temperature. All potentials were *iR*-compensated and converted to a reversible hydrogen electrode (RHE) scale with following equation: $E_{(RHE)} = E_{(SCE)} + (0.241 + 0.059 \times pH)$. And the presented current density was normalized to the geometric surface area.

DFT calculations. The spin-polarized periodic DFT calculations of the atomic structure and electronic structure are performed by using Vienna ab initio simulation (VASP)[1,2]. The interaction is described by projector augmented wave (PAW) method[3] with Perdew-Burke-Ernzerh (PBE) functional[4]. The energy cutoff for wave function is 400 eV. The exchange correlation energy and potential are described by generalized gradient approximation (GGA) in the form of Perdew-Burke-Ernzerhof (PBE)[4]. Plane waves are used to expand wave functions with a cutoff of 400 eV for projector augmented wave (PAW) potentials[3]. To decrease the interaction between neighboring unit cells, the supercell of protonated hexacyanocobaltate(III), tetracyanoplatinate(II), PANI, and their hybrids are expanded to 24.99*20.54*20.02 Å compared to our previous work, and the optimized PANI unit of 20.54 Å agrees well with the previous work of 20.53 Å[5]. The

K-points grids are 1x1x1 for all structures, and the atomic positions are full relaxed until the residual force is less than 0.03 eV/Å. The reaction process of PANI-metal complex ions were calculated by two steps: the protonation energy of redox units of PANI and the bonding energy between protonated PANI and metal complex ions. To maintain neutral electricity of the system, the metal complex ions are also partially protonated. Spin polarization is considered during all the calculations.

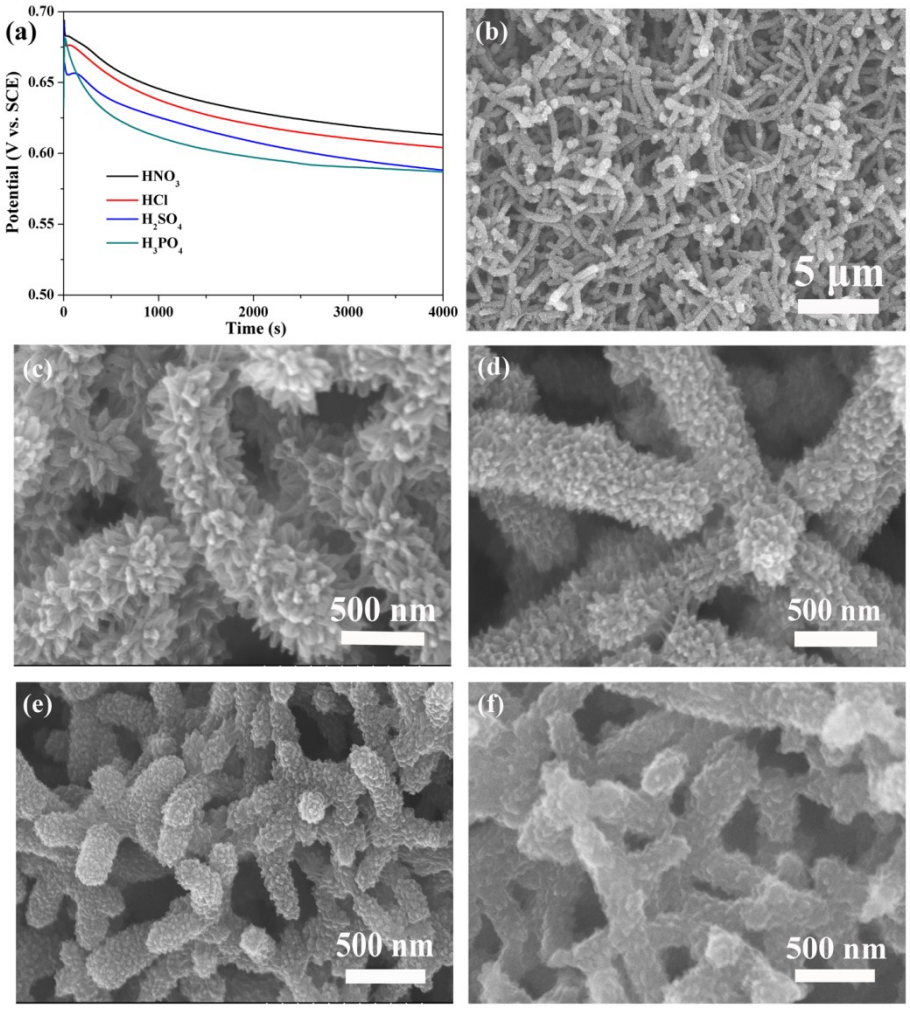

Fig. S1 (a) V-t curves for electrochemical polymerization of PANI by galvanostatic method at a current density of 2 mA cm^{-2} for 4000 s on carbon paper. (b)-(f) SEM images of PANI prepared by using different acid electrolytes: (b) and (c) HNO_3, (d) HCl, (e) H_2SO_4, and (f) H_3PO_4.

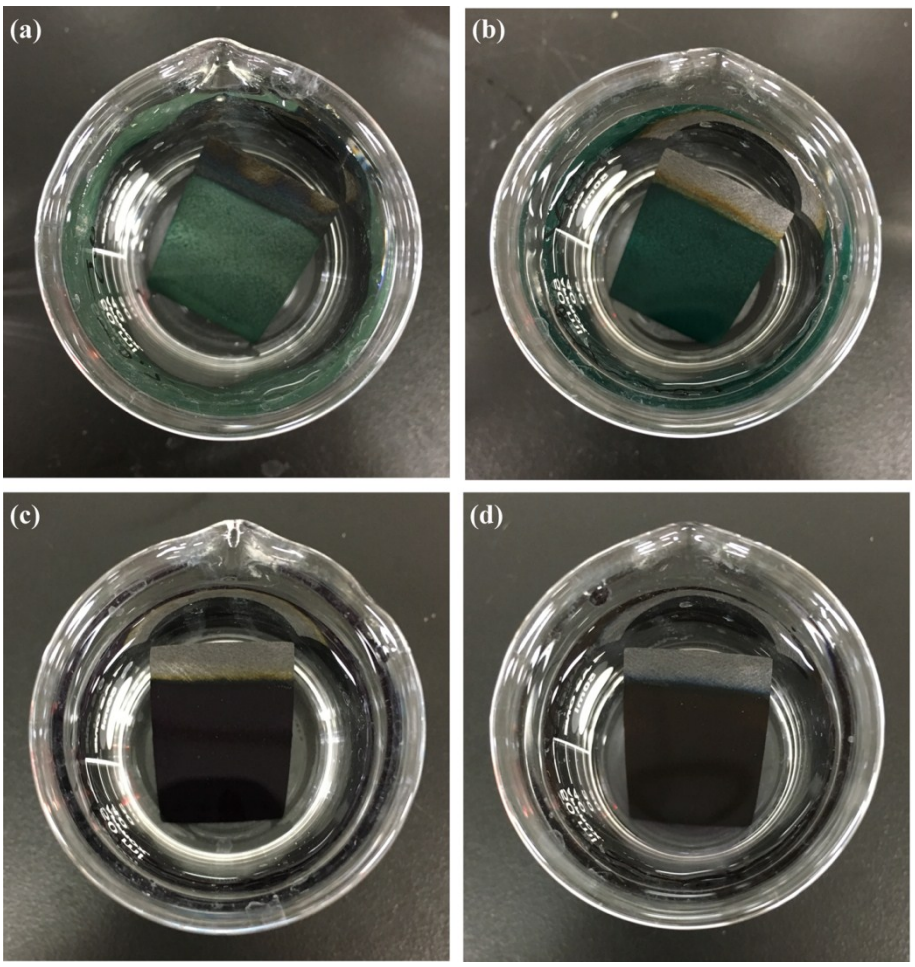

Fig. S2 Photographs of PANIs treated at different potentials by the potentiostatic method: (a) -0.5 V, (b) 0 V, (c) 0.45 V, and (d) 0.8 V vs. SCE.

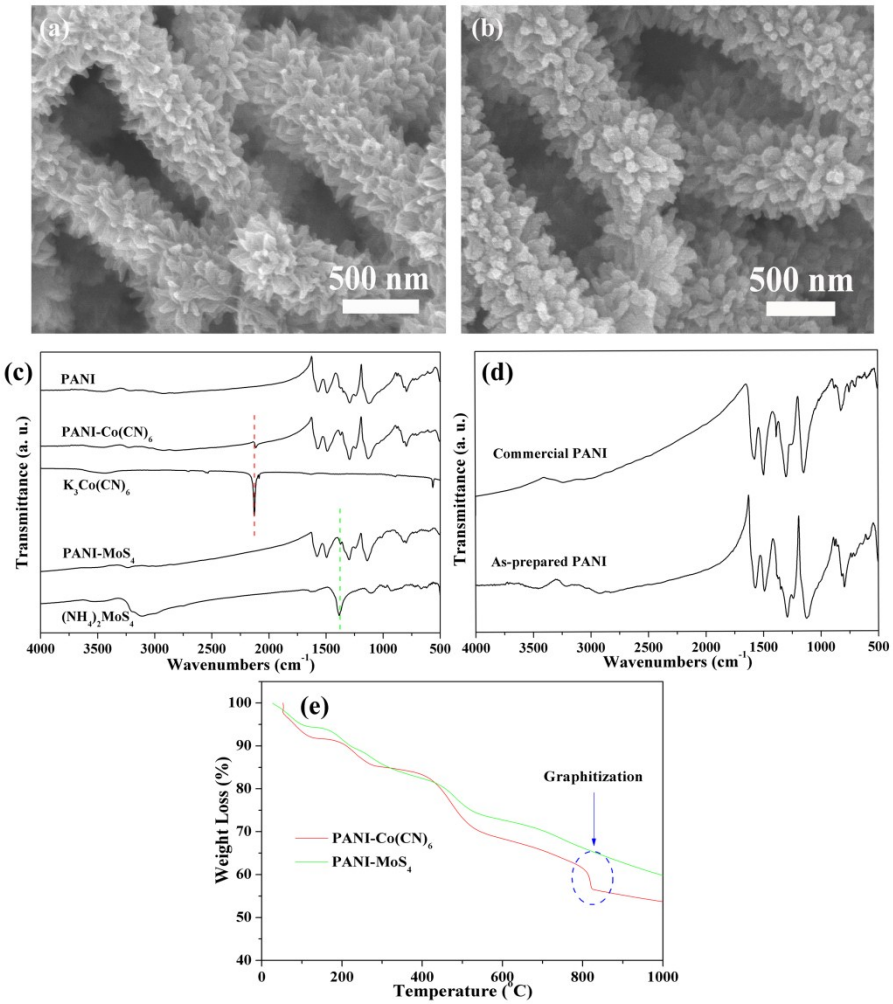

Fig. S3 SEM images of 0.45 V treated PANI/metal complex ion composites: (a) PANI-$Co(CN)_6$ and (b) PANI-MoS_4. (c) Comparison of FTIR of pure PANI, composites and pure metal salts. (d) Comparison of FTIR of as-prepared PANI and commercial PANI. The main peaks are almost same and similar with the literature,[6] indicating no other polymers are produced during electrochemical polymerization. (e) TG curves of the two composites. During carbonization process, there is an obvious graphitization reaction in Co-based composite precursor.

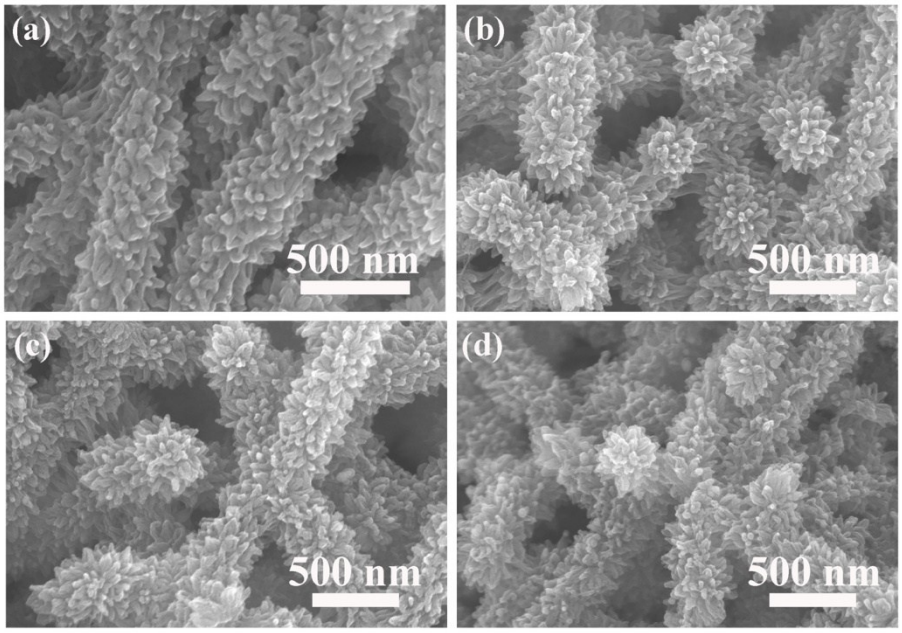

Fig. S4 SEM images of Co@NC samples derived from different potentials treated PANI: (a) Co@NC(-0.5), (b) Co@NC(-0.2), (c) Co@NC(0), and (d) Co@NC(0.8).

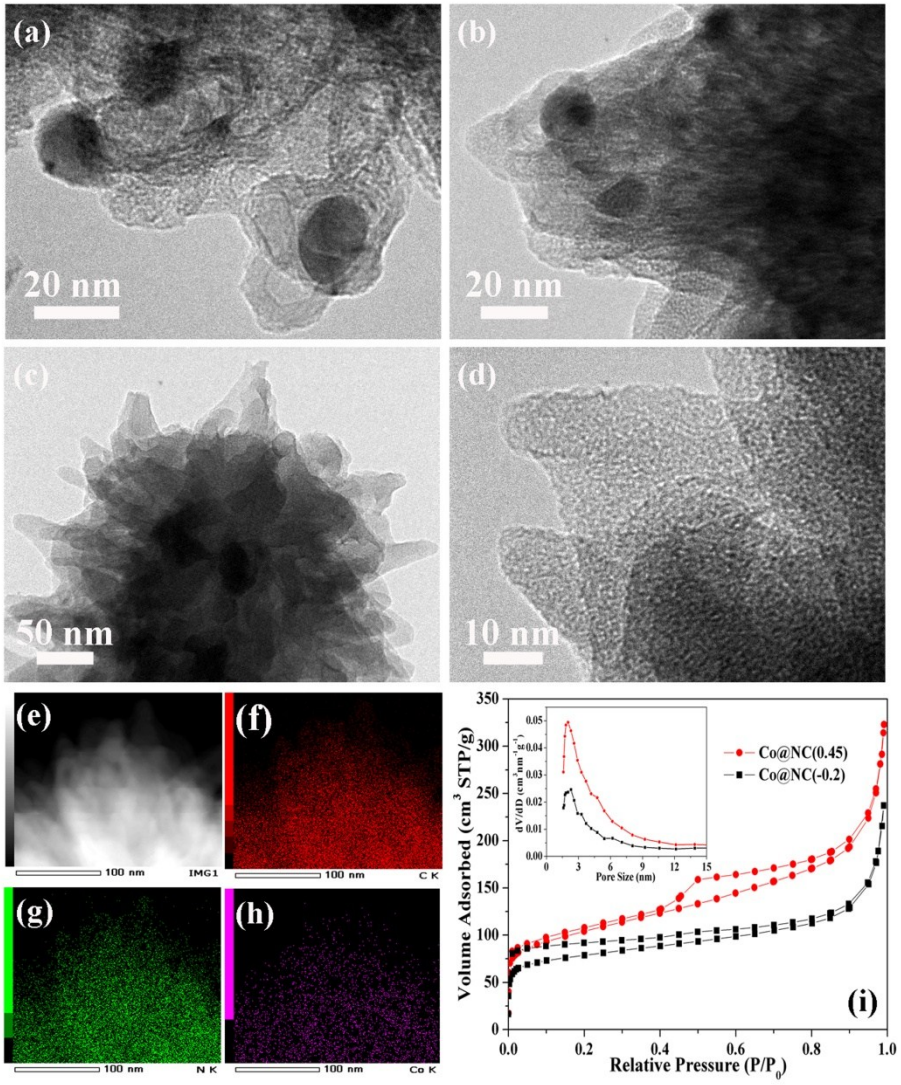

Fig. S5 TEM images of Co@NC samples: (a) and (b) Co@NC(0.45), (c) and (d) Co@NC(-0.2). (e)-(h) EDX mapping of Co@NC(-0.2): (e) STEM image, (f) C, (g) N, and (h) Co elements mapping. (i) Nitrogen adsorption-desorption curves and their corresponding pore size distributions of Co@NC(0.45) and Co@NC(-0.2).

For Co@NC(-0.2), the metal particles are not observed even at the high magnification (Fig. S5c, d), which may be due to the low metal content. EDX spectrum analysis shows that the Co metal atom is homogeneously distributed over the entire material even low metal loading, indicating that the metal complexes are uniformly bonded to PANI at different redox states (Fig. S5e-h). The N_2 sorption isotherms of Co@NC(-0.2) exhibits type I isotherms, and rapid N_2 uptake in the low-pressure region indicates the presence of micropores (less than 2 nm) (Fig. S5i). The specific surface areas is 215 m^2 $g^{-1}$for Co@NC(-0.2).

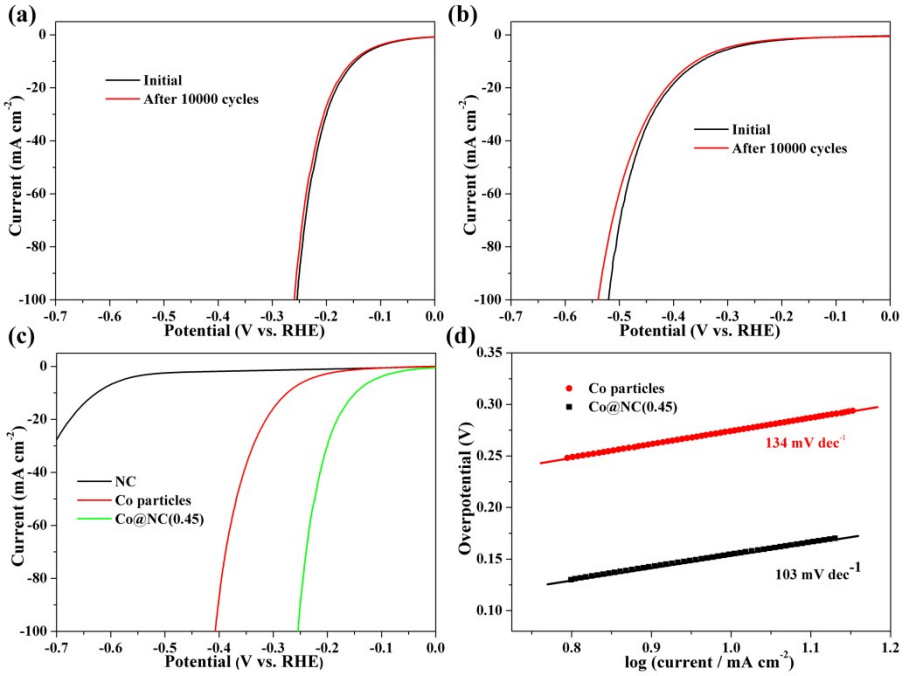

Fig. S6 (a) Cycle stability measurement of Co@NC(0.45). (b) Cycle stability measurement of COM Co/NC. (c) Polarization curves and (d) Tafel plots of Co particles and Co@NC(0.45).

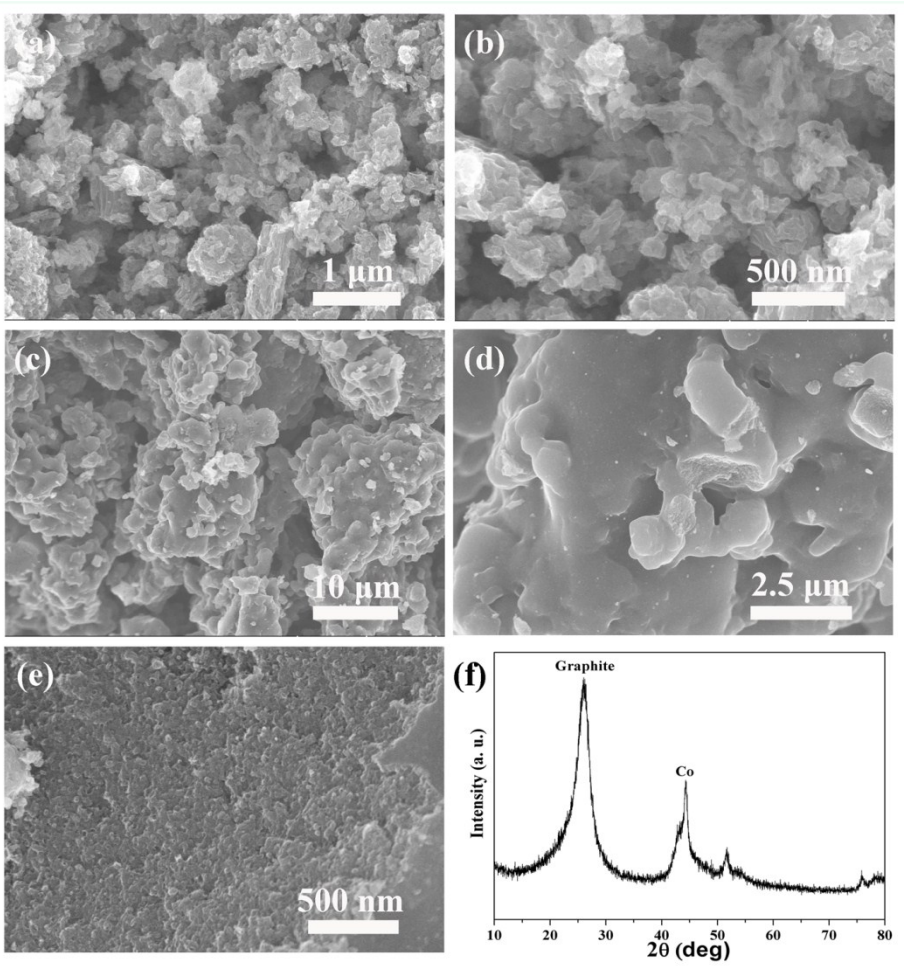

Fig. S7 (a) and (b) SEM images of commercial PANI/$Co(CN)_6$ precusor. (c)-(e) Carbonized product of commercial PANI/$Co(CN)_6$ at 900 C for 3h (COM Co/NC). (f) XRD pattern of COM Co/NC.

The morphologies of commercial PANI are irregular particles (Fig. S7a, b) and after carbonization, small particles are aggregated into large particles of tens of micrometers (Fig. S7c-d), which suggest that the structures of commercial PANI are very unstable during thermal treatment. In contrast, the structures of our hierarchically-ordered and integrated PANI are very stable during carbonization and the morphologies nearly no change except the shrinkage from pyrolysis. By comparison, it highlights the unique advantages of our synthesis strategy.

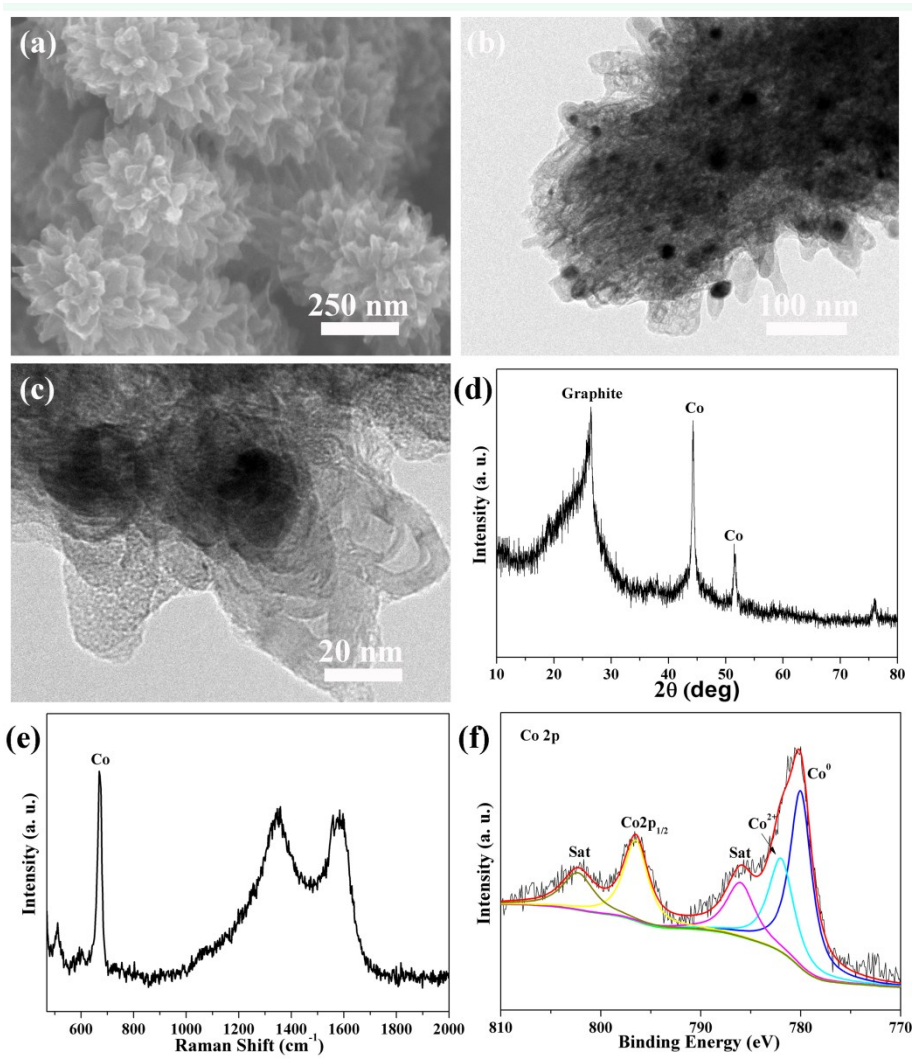

Fig. S8 (a) SEM image, (b) and (c) TEM images, (d) XRD pattern, (e) Raman spectra, and (f) Co 2p XPS spectra of Co@NC(0.45) after HER test.

From the SEM and TEM images (Fig. S8a-c), it can be seen that the hierarchically-ordered nanostructures are well maintained during HER test. The XRD, Raman, and XPS spectra (Fig. S8d-f) clearly show the strong peaks of metal Co, similar to the ones before test, indicating the excellent stability of the Co@NC(0.45) catalyst.

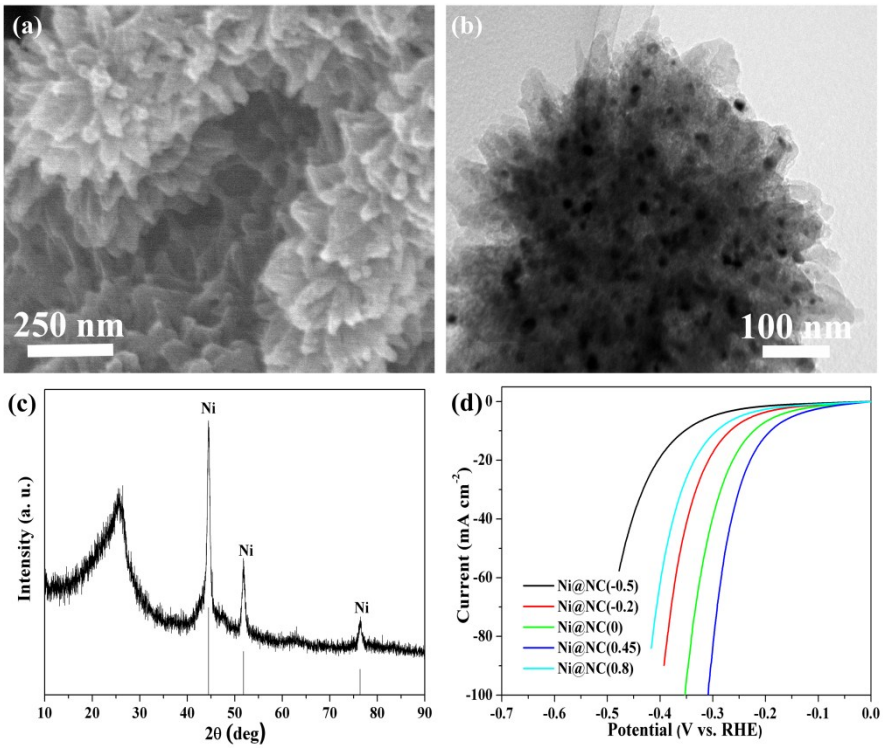

Fig. S9 (a) SEM image, (b) TEM image, and (c) XRD pattern of Ni@NC(0.45). (d) HER performance of a series of Ni@NC samples.

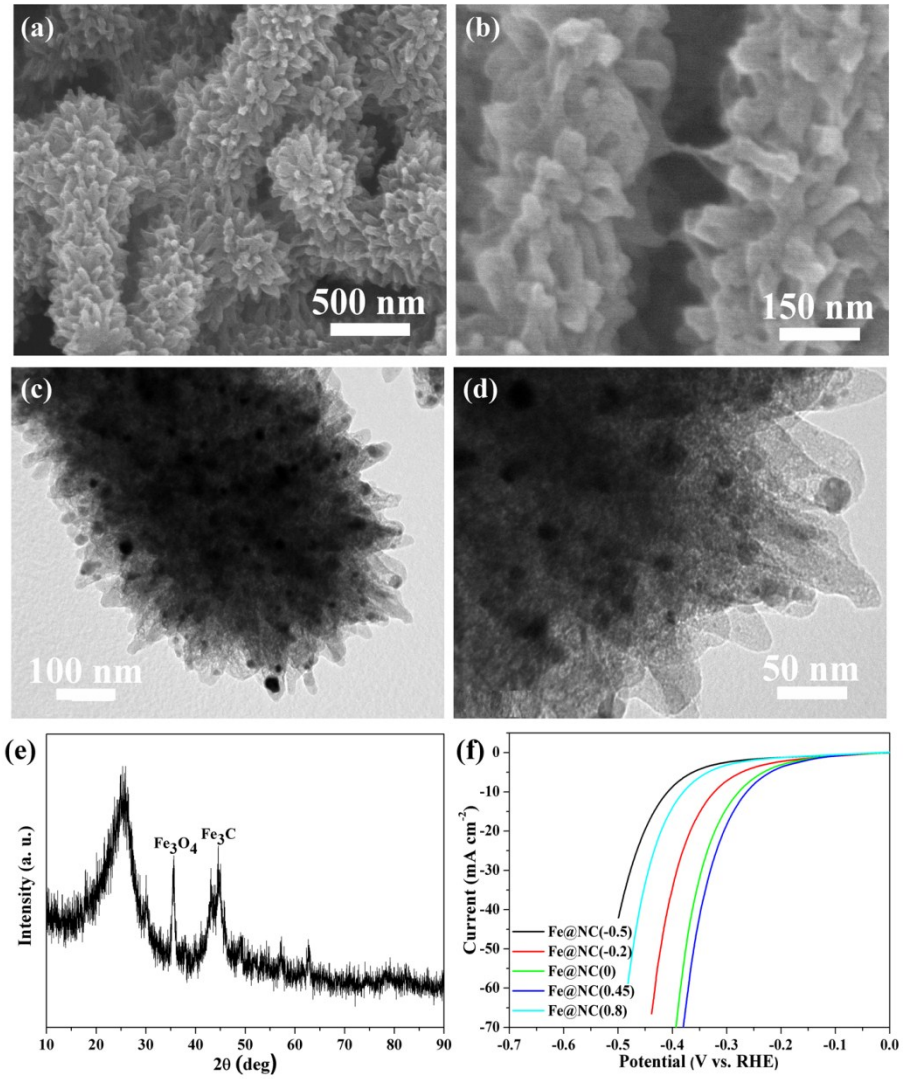

Fig. S10 (a) and (b) SEM images, (c) and (d) TEM images, and (e) XRD pattern of Fe@NC(0.45). (f) HER performance of a series of Fe@NC samples.

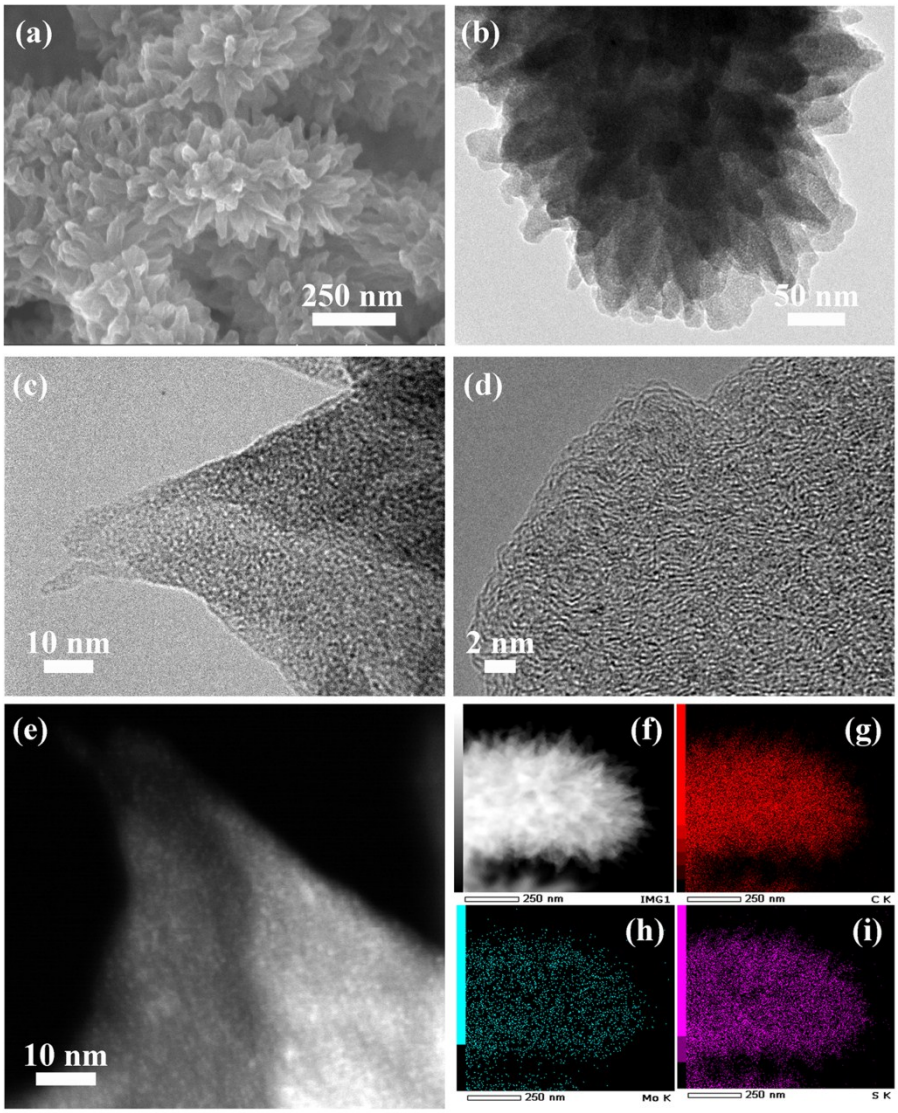

Fig. S11 (a) SEM image, (b) and (c) TEM images, (d) HRTEM image, (e) High-magnification STEM image, (f)-(i) EDX mapping of MoC_xS_y@NC(-0.1): (f) STEM image, (g) C, (h) Mo, and (i) S elements mapping.

From the SEM and TEM images (Fig. S11a and b), it can be seen that MoC_xS_y@NC(-0.1) retains the 3D structure with branched carbon fibers after MoC_xS_y deposition and carbonization. Interestingly, on the edge of the branched needles, no crystalline particles are observed even in the HRTEM image (Fig. S11d). However, in the STEM image (Fig. S11e), it can be found that ultrasmall nanoparticles are uniformly coated on the carbon surface, which indicating the amorphous nature of MoC_xS_y nanoparticles. EDX mapping shows that the Mo and S atoms are homogeneously distributed over the entire carbon fiber (Fig. S11f-i).

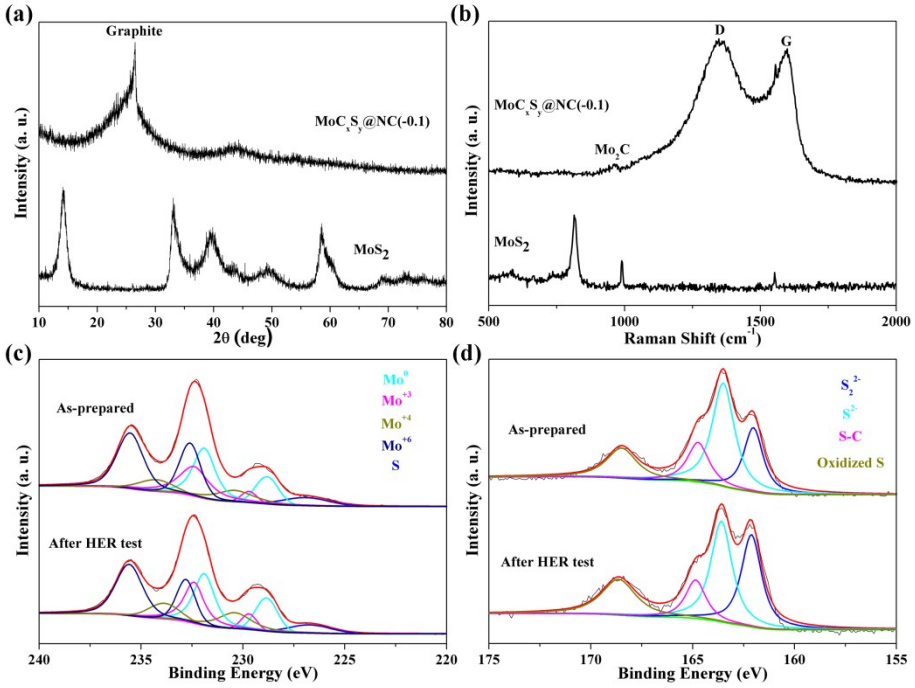

Fig. S12 (a) XRD and (b) Raman spectra of MoC_xS_y@NC(-0.1) sample and pure $(NH_4)_2MoS_4$ derived MoS_2. (c) Mo 3d and (d) S 2p XPS spectra of MoC_xS_y@NC(-0.1) before and after HER test.

In the XRD pattern (Fig. S12a), there is no peaks of Mo-based compounds in the MoC_xS_y@NC(-0.1) sample and in the Raman spectra (Fig. S12b), there is a small peak around 960 cm^{-1}, which may be from a small amount of Mo_2C.[7] The intensity ratio between D and G bands (I_D/I_G) was found to be 1.1, which suggests the presence of significant structural defects within the carbon layer. Fig. S12c shows the peak-fitted curves of the XPS Mo 3d spectrum, in which the peaks correspond to Mo^0, Mo^{3+}, Mo^{4+}, and Mo^{6+} species. The presence of Mo^0 suggests Mo-C bond formation. In Fig. S12d, the S 2p3/2 at 162.0 eV can be attributed to terminal S_2^{2-} ligands, and the S 2p1/2 at 163.5 eV represents apical S^{2-} ligands. The shoulder peak at 165 eV indicates the formation of S-C bonding. The ratio of S to Mo is calculated to be approximately 1.07 from the XPS analysis. Combined all the results, it can be concluded that the pyrolysis of PANI-MoS_4 precursor under high temperature produce a Mo-C-S hybrid structures. The Mo atoms have strong affinity to C, so when pyrolysis of PANI-MoS_4 precursor, Mo atoms will prefer to stay in the carbonaceous matrix.[8] This is why direct pyrolysis of $(NH_4)_2MoS_4$ produces pure MoS_2 but PANI-MoS_4 precursor cannot. However, it is difficult to accurately determine its chemical formula of Mo-C-S, which is a very complex system. So we use MoC_xS_y to represent this compound. After HER test, the peaks of Mo^0 and S^{2-} are slightly enhanced, indicating that a small amount of high-valence ions are reduced. Mo^{6+} and oxidized organic S are likely to be generated by interactions with little impurity O_2 or entrapped O from the PANI host during carbonization.

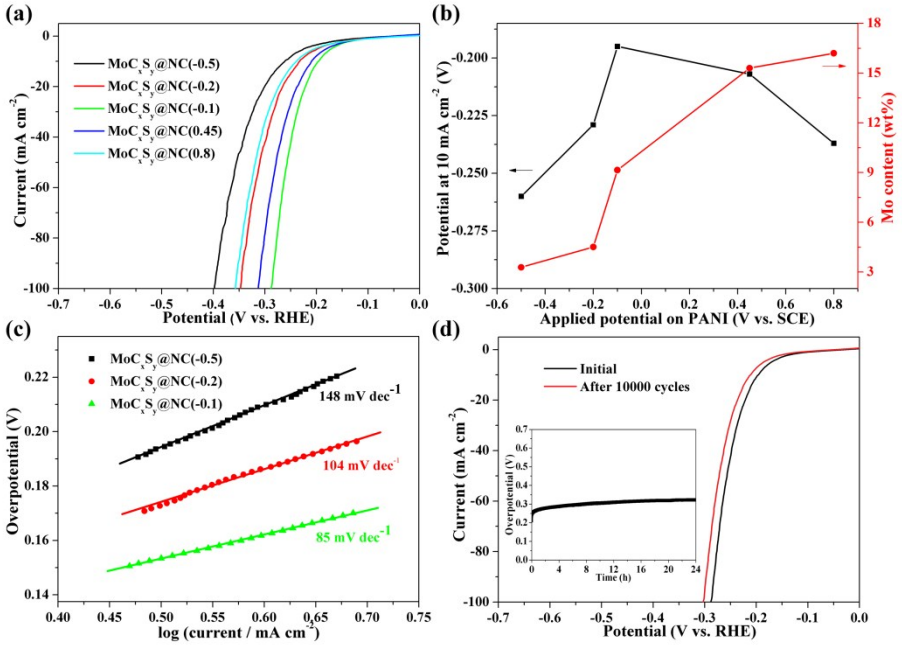

Fig. S13 (a) Polarization curves of a series of MoC_xS_y@NC samples prepared by applying different potentials on PANI from -0.5 V to 0.8 V. (b) Potentials at 10 mA cm^{-2} and metal (Mo) content as a function of the applied potentials. (c) Tafel plots of MoC_xS_y@NC(-0.5), MoC_xS_y@NC(-0.2) and MoC_xS_y@NC(-0.1). (d) Cycle stability measurement of MoS_x@NC(-0.1). Inset in (d) is chronopotentiometric curves of MoC_xS_y@NC(-0.1) with constant current densities of 50 mA cm^{-2}.

The HER activity of MoC_xS_y@NC samples were conducted in 0.5 M H_2SO_4 solution. The activities first increase rapidly and then slightly decrease with higher applied potentials from -0.5 V to 0.8 V (Fig. S13a and b). For MoC_xS_y@NC(0.45) and MoC_xS_y@NC(0.8), the Mo contents in both samples are higher than MoC_xS_y@NC(-0.1), but their activities become lower. High loading may produce large particles, which leads to a lower active surface area and decreases the activity. Among the MoC_xS_y@NC samples, MoC_xS_y@NC(-0.1) exhibits the best activity. It shows an overpotential of 195 mV at 10 mA cm^{-2} and a Tafel slope of 85 mV dec^{-1} with excellent durability (Fig. S13c and d).

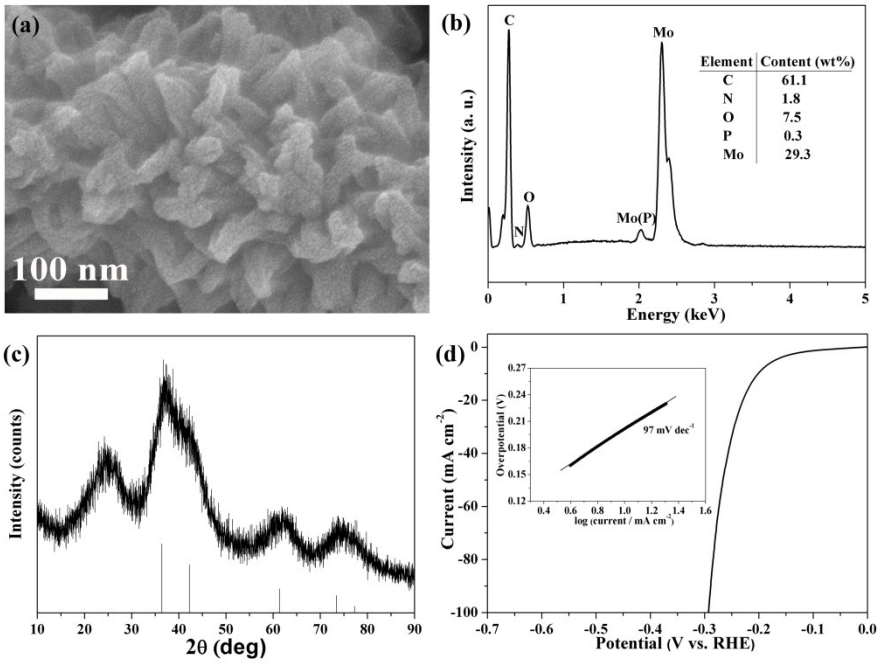

Fig. S14 (a) SEM image, (b) EDX spectrum, (c) XRD pattern, and (d) HER performance of MoC@NC(0.45).

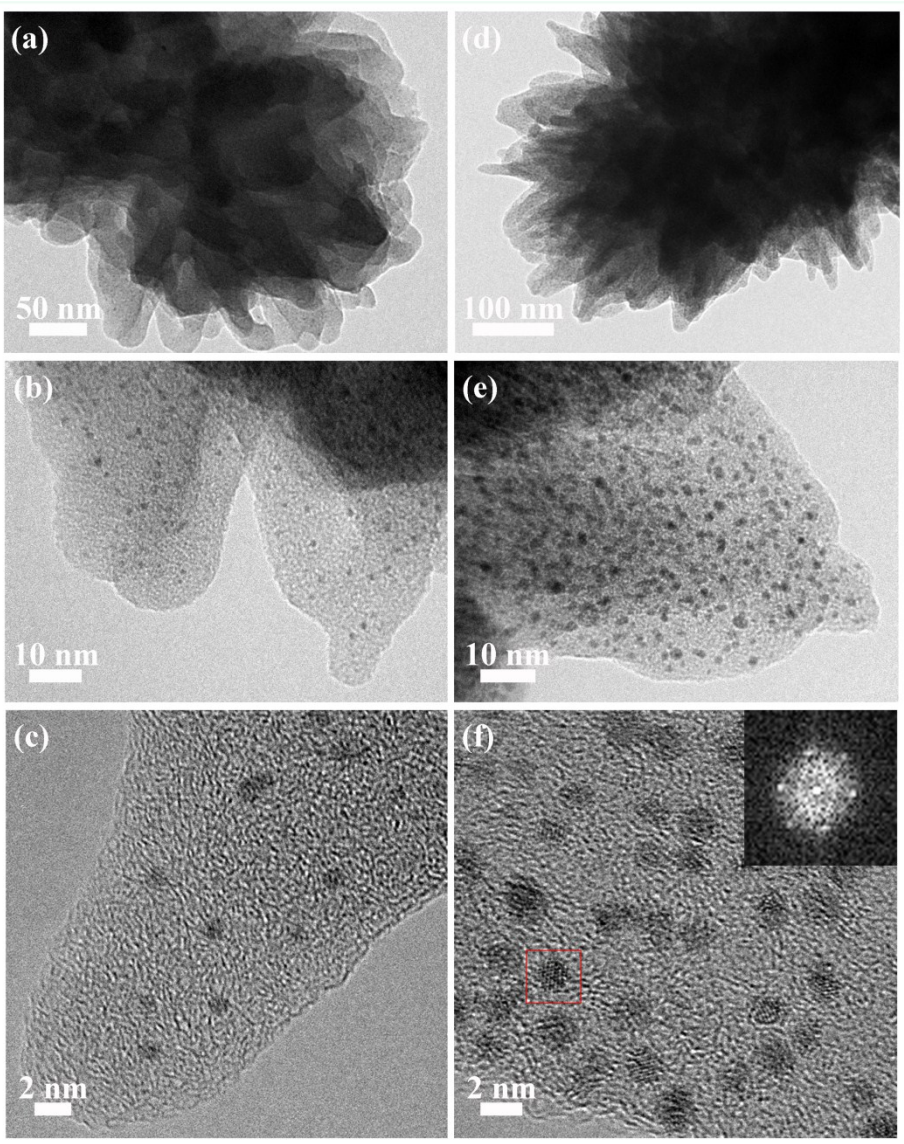

Fig. S15 Comparison of TEM and HRTEM images of Pt@NC(-0.5) (a)-(c) and Pt@NC(0.45) (d)-(f).

From Pt@NC(-0.5) to Pt@NC(0.45), the concentrations of Pt increase from 5.5 to 25.0 wt%. Obviously, in the TEM and HRTEM images (Fig. S15a-f), the density of Pt nanoclusters increased from Pt@NC(-0.5) to Pt@NC(0.45), and particle sizes become a little larger from ~1.5 nm in Pt@NC(-0.5) to ~2.5 nm in Pt@NC(0.45).

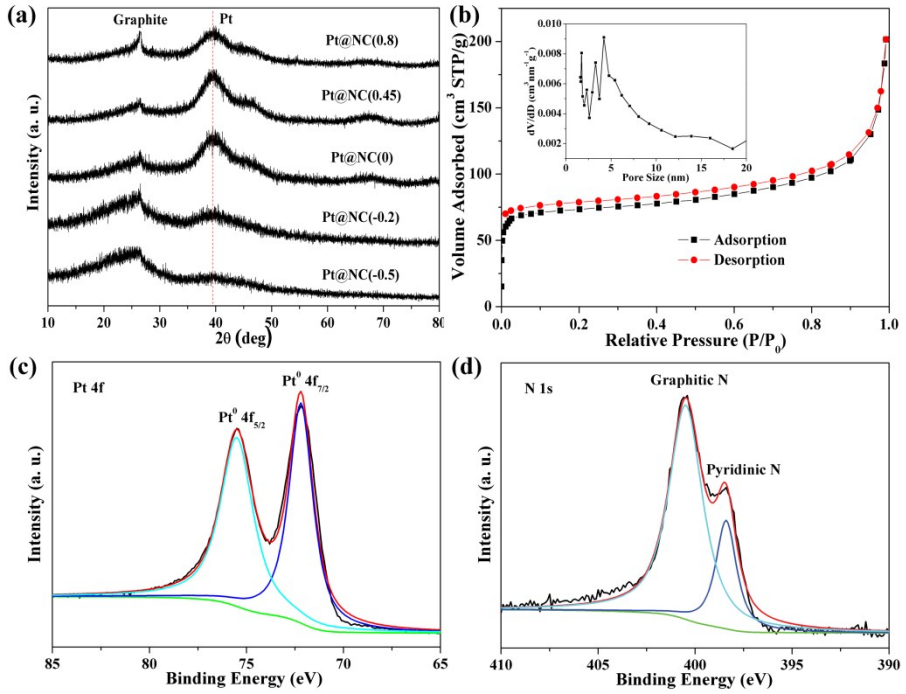

Fig. S16 (a) XRD patterns of the Pt@NC samples. (b) Nitrogen adsorption-desorption curves and their corresponding pore size distributions, (c) Pt 4f, and (d) N 1s XPS spectra of Pt@NC(-0.2).

The N_2 sorption isotherms of Pt@NC(-0.2) has type I isotherms, and rapid N_2 uptake in the low-pressure region indicates the presence of micropores (less than 2 nm). The specific surface areas is 253 m^2 $g^{-1}$for Pt@NC(-0.2). XPS of Pt 4f reveals two clear distinct peaks at 72.1 and 75.4 eV as shown in Fig. 16c, corresponding to Pt^0 $4f_{5/2}$ and Pt^0 $4f_{7/2}$, respectively. In the N 1s spectra (Fig. S16d), two peaks are fitted at binding energy of 398.4 and 400.5 eV, corresponding to the pyridinic N and graphitic N, respectively. Compared to the XPS of commercial Pt/C reported in the literature,[9] there is an obvious positive shift (about 0.7 eV) in the binding energies of Pt 4f. Interestingly, in the N 1s spectra, there is a corresponding negative shift (about 0.4 eV). These shifts in binding energy could be ascribed to the electronic interaction between the Pt nanoclusters and the N-doped carbon support, which would a□ect the electronic structures of the surface Pt atoms and improve the catalytic performance.[10]

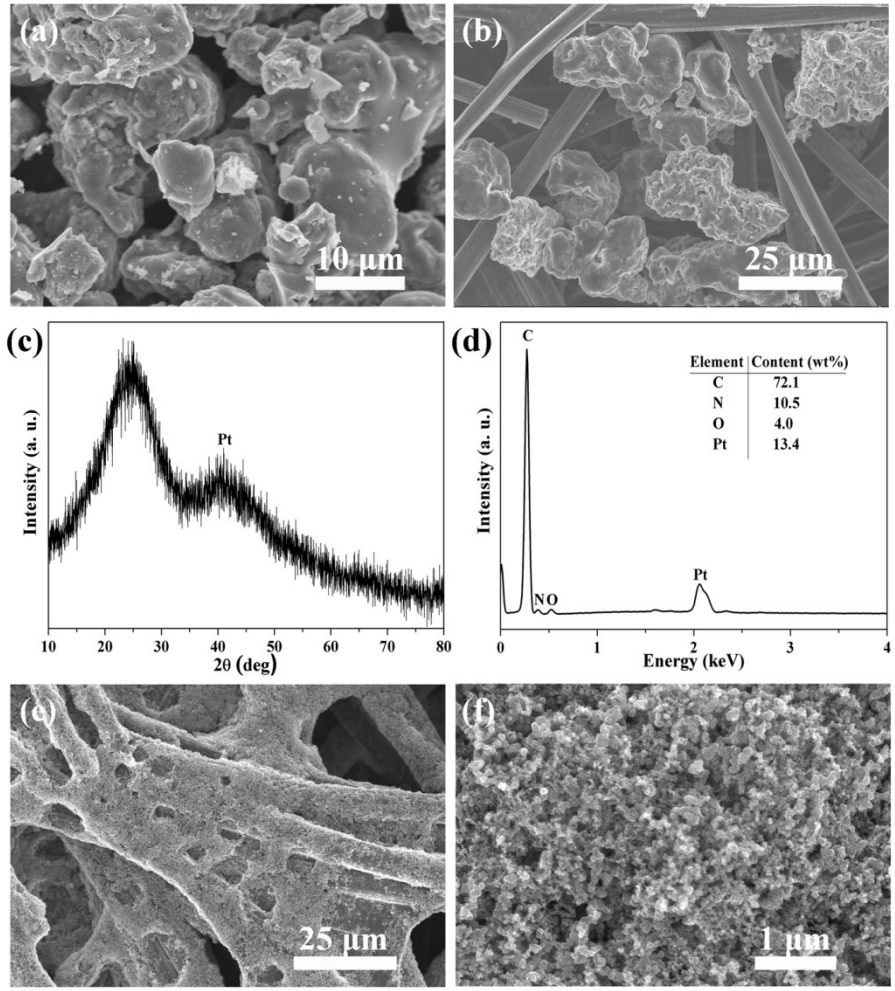

Fig. S17 (a) SEM image of commercial PANI/$Pt(CN)_4$ precusor derived Pt/NC sample (COM Pt/NC). (b) COM Pt/NC based electrode structure. (c) XRD pattern and (d) EDX spectrum of COM Pt/NC. (e) and (f) Commercial 20% Pt/C (COM 20% Pt/C) based electrode structures. Both electrodes are prepared by conventional method that powders and Nafion are mixed in ethanol and dropped on CP.

Like COM Co/NC, commercial PANI derived Pt/NC sample also form very large particles even at 700 ^{o}C (for Co/NC, at 900 ^{o}C), further confirming the structural instability with serious aggregation of commercial PANI. The XRD pattern demonstrates the formation of metal Pt and the EDX shows the high concentration with 13.4 wt%. Fig. S17e and f show the morphologies of commercial 20% Pt/C (COM 20% Pt/C) based electrode structures. Obviously, the catalyst particles are seriously agglomerated together, which is extremely unfavorable for the transport of reactants.

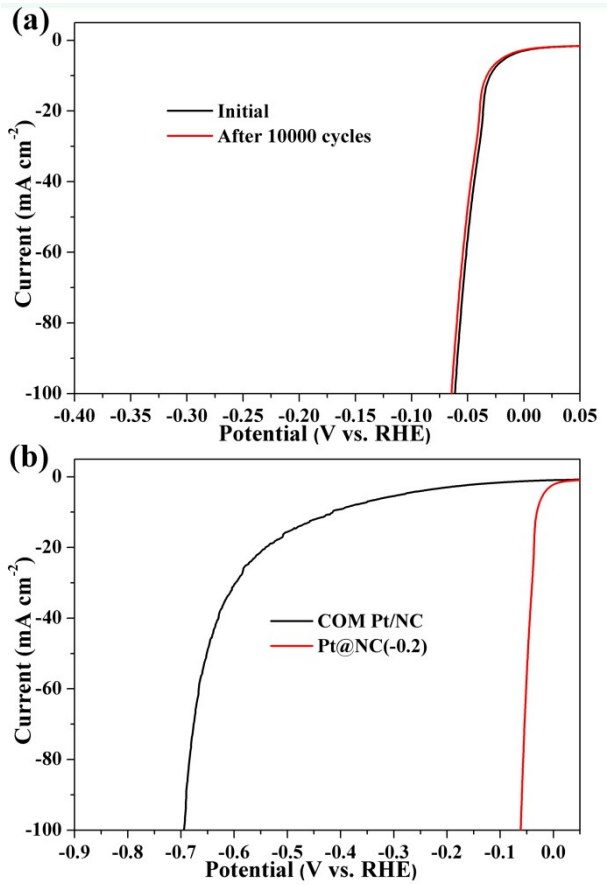

Fig. S18 (a) Cycle stability measurement of Pt@NC(-0.2). (b) Polarization curves of COM Pt/NC and Pt@NC(-0.2).

Pt@NC(-0.2) exhibits super cycle stability and after 10000 cycles, the overpotential only decreases about 3 mV (Fig. S18a). Although the Pt concentration of commercial PANI derived Pt/C (COM Pt/NC) is very higher than Pt@NC(-0.2), it exhibits very bad performance compared to Pt@NC(-0.2) (Fig. S18b) due to the serious aggregation structures and Pt almost doesn't play any roles, which indirectly imply the importance of the hierarchically ordered structure in Pt@NC(-0.2).

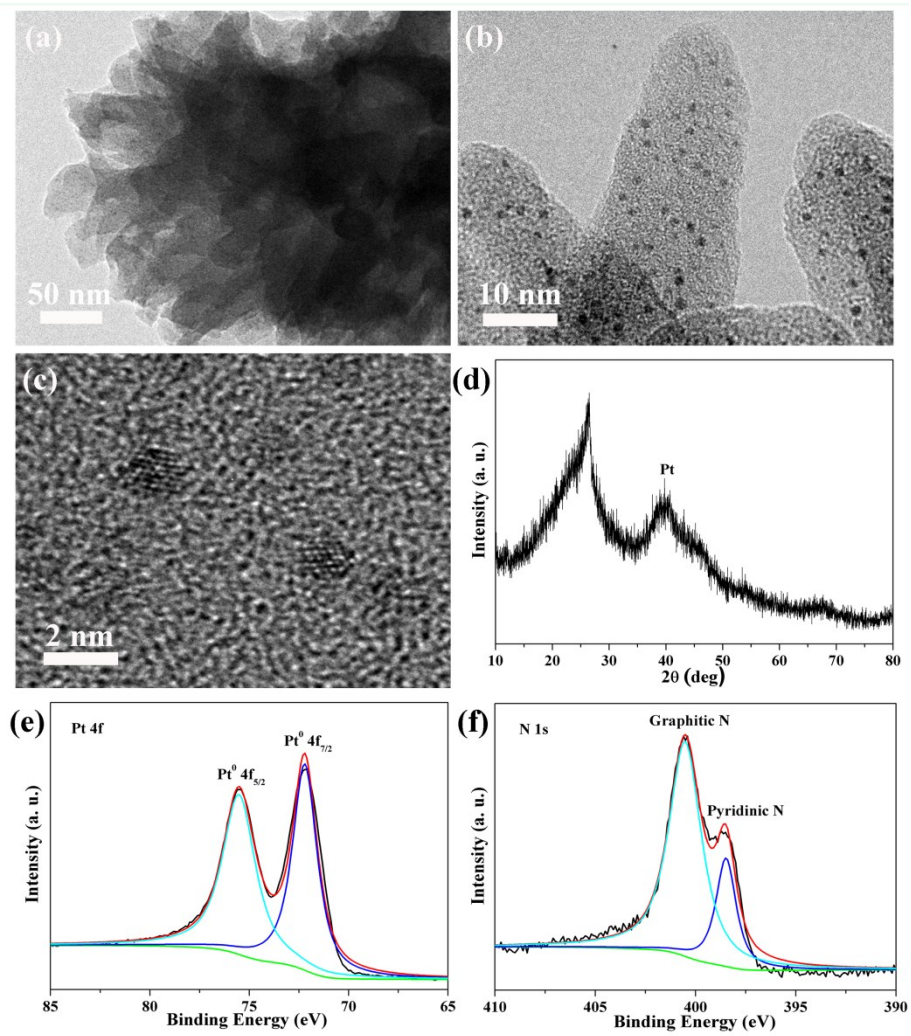

Fig. S19 (a) and (b) TEM images, (c) HRTEM image, (d) XRD pattern, (e) Pt 4f, and (f) N 1s XPS spectra of Pt@NC(-0.2) after HER test.

From the TEM images (Fig. S19a-c), it can be seen that the Pt nanoclusters remain uniformly dispersed during HER test. The XRD and XPS spectra (Fig. S19d, e) clearly show the strong peaks of metal Pt, similar to the ones before test, indicating the excellent stability of the Pt@NC(-0.2) catalyst.

Table S1. Comparison of representative carbon-based and other non-noble metal HER catalysts in alkaline electrolyte.

Catalyst	Current density (j, mA cm^{-2})	Overpotential at the corresponding j (mV)	Tafel slope (mV dec^{-1})	Reference
Co@NC	1	40	103	***This work***
	10	145		
Co-S/FTO	1	480	-	*J. Am. Chem. Soc.*, 2013, **135**, 17699-17702.
Co-NRCNTs	1	160	-	*Angew. Chem. Int. Ed.*, 2014, **53**, 4372-4376.
	10	370		
CoP/CC	1	115	129	*J. Am. Chem. Soc.*, 2014, **136**, 7587-7590
	10	209		
Co phosphide /phosphate film	30	430	-	*Adv. Mater.*, 2015, **27**, 3175-3180.
CoO_x@CN	10	232	115	*J. Am. Chem. Soc.*, 2015, **137**, 2688-2694.
CoN_x/C	10	170	75	*Nat. Commun.*, 2015, **6**, 7992.
Co-NGs	10	270	-	*Nat. Commun.*, 2015, **6**, 8668.
Co-C-N	10	178	102	*J. Am. Chem. Soc.*, 2015*,* **137***, 15070-15073.*
Co@BCN	10	183	73.2	*ACS Nano*, 2016, **10**, 684-694.
Co_2P@NPG	10	165	96	*Nano Lett.*, 2016, **16**, 4691-4698.
c-$CoSe_2$/CC	10	190	85	*Adv. Mater.*, 2016, **28**, 7527-7532.
Co/NBC-900	10	117	146	*Adv. Funct. Mater.*, 2018, **28**, 1801136.
NiCoP/rGO	10	209	124	*Adv. Funct. Mater.*, 2016, **26**, 7644-7651.
Ni	10	400	-	*Angew. Chem. Int. Ed.*, 2012, **51**, 12703-12706.
MoB	10	225	59	*Angew. Chem. Int. Ed.*, 2012, **51**, 12703-12706.
Ni wire	10	350		*ACS Catal.*, 2013, **3**, 166-169.
MoC	10	250	-	*Energy Environ. Sci.*, 2014, **7**, 387-392.
WC@CNS	10	220	-	*J. Am. Chem. Soc.*, 2015, **137**, 5480-5485.
MoC_x	10	151	59	*Nat. Commun.*, 2015, **6**, 6512.
$NiMo_3S_4$	10	257	98	*Angew. Chem. Int. Ed.*, 2016, **55**, 15240-15245.
Mo-SAC	10	132	90	*Angew. Chem. Int. Ed.* **2017**, *56*, 16086-16090.
NiS_2 porous hollow microspheres	10	174	82	*ACS Appl. Mater. Interfaces*, 2017, **9**, 2500-2508.
Cu NDs/Ni_3S_2 NTs-CFs	10	128	76.2	*J. Am. Chem. Soc.*, 2018, **140**, 610-617.

Table S2. Comparison of representative noble metal Pt/Ru-based HER electrocatalysts in alkaline electrolyte.

Catalyst	Current density (j, mA cm^{-2})	Overpotential at the corresponding j (mV)	Tafel slope (mV dec^{-1})	Reference
Pt@NC	10	28	28	***This work***
	100	61		
Pt-(PtO_x)-NSs/C	10	53	65	*ChemSusChem*, 2018, 11, 2388-2401.
	20	81		
Pt-Ni ASs	10	27.7	27	*Adv. Mater.*, 2018, 1801741.
	30	53.8		
Pt_3Ni_2-NWs-S/C	10	42	-	*Nat. Commun.*, 2017, **8**, 14580.
PtNi alloy nanomultipods[a]	22	70	78	*Nat. Commun.*, 2017, **8**, 15131.
NiO_x/Pt_3Ni Pt_3Ni_3-NWs	10	40	-	*Angew. Chem. Int. Ed.*, 2016, **55**, 12859-12863.
PtNWs /SLNi$(OH)_2$	4	85.5	-	*Nat. Commun.*, 2015, **6**, 6430.
Ru/C_3N_4/C[a]	10	79	~ 69	*J. Am. Chem. Soc.*, 2016, **138**, 16174-16181.
Ru@C_2N	10	17	38	Nat. Nanotechnol., 2017, **12**, 441-446.
	30	~ 50		

[a] The basic electrolyte is 0.1 M KOH solution. Others are all 1 M KOH solution.

References

1 P. Kackell, J. Furthmuller, F. Bechstedt, G. Kresse, J. Hafner, *Phys. Rev. B*, 1996, **54**, 10304-10307.

2 G. Kresse, J. Furthmüller, *Comp. Mater. Sci.*, 1996, **6**, 15-50.

3 J. J. Mortensen, L. B. Hansen, K. W. Jacobsen, *Phys. Rev. B*, 2005, **71**, 035109.

4 J. P. Perdew, K. Burke, M. Ernzerhof, *Phys. Rev. Lett.*, 1996, **77**, 3865-3868.

5 R. X. Wang, L. F. Huang, X. Y. Tian, *J. Phys. Chem. C*, 2012, **116**, 13120-13126.

6 E. T. Kang, K. G. Neoh, K. L. Tan, *Prog. Polym. Sci.*, 1998, **23**, 277-324.

7 Y. P. Liu, G. T. Yu, G. D. Li, Y. H. Sun, T. Asefa, W. Chen, X. X. Zou, *Angew .Chem. Int. Ed.*, 2015, **54**, 10752-10757.

8 T. Wang, H. K. Kim, Y. Liu, W. Li, J. T. Gri□ths, Y. Wu, S. Laha, K. D. Fong, F. Podjaski, C. Yun, R. V. Kumar, B. V. Lotsch, A. K. Cheetham, S. K. Smoukov, *J. Am. Chem. Soc.*, 2018, **140**, 6130-6136.

9 J. Melke, B. Peter, A. Habereder, J. Ziegler, C. Fasel, A. Nefedov, H. Sezen, C. Wöll, H. Ehrenberg, C. Roth, *ACS Appl. Mater. Interfaces*, 2016, **8**, 82-90.

10 L. Guo, W. J. Jiang, Y. Zhang, J. S. Hu, Z. D. Wei, L. J. Wan, *ACS Catal.*, 2015, **5**, 2903-2909.